

Depth-sensitive reflectance measurements using obliquely oriented fiber probes

Adrien Ming Jer Wang

Janelle Elise Bender

Rice University
Department of Bioengineering
Houston, Texas

Joshua Pfefer

Food and Drug Administration
Center for Devices and Radiological Health
Rockville, Maryland

Urs Utzinger

University of Arizona
Biomedical Engineering Program and OB/GYN
Tucson, Arizona

Rebekah Anna Drezek

Rice University
Department of Bioengineering
Houston, Texas
E-mail: drezek@rice.edu

Abstract. Computer simulation is used to facilitate the design of fiber-probe geometries that enable enhanced detection of optical signals arising from specific tissue depths. Obtaining understanding of the relationship between fiber-probe design and tissue interrogation is critical when developing strategies for optical detection of epithelial precancers that originate at known depths from the tissue surface. The accuracy of spectroscopic diagnostics may be enhanced by discretely probing the optical properties of epithelium and underlying stroma, within which the morphological and biochemical features vary as a function of depth. While previous studies have investigated controlling tissue-probing depth for fluorescence-based modalities, in this study we focus on the detection of reflected light scattered by tissue. We investigate how the depth of optical interrogation may be controlled through combinations of collection angles, source-detector separations, and numerical apertures. We find that increasing the obliquity of collection fibers at a given source-detector separation can effectively enhance the detection of superficially scattered signals. Fiber numerical aperture provides additional depth selectivity; however, the perturbations in sampling depth achieved through this means are modest relative to the changes generated by modifying the angle of collection and source-detection separation. © 2005 Society of Photo-Optical Instrumentation Engineers. [DOI: 10.1117/1.1989335]

Keywords: fiber optic probes; reflectance spectroscopy; epithelial tissue; Monte Carlo.

Paper 04146RRR received Jul. 29, 2004; revised manuscript received Mar. 16, 2005; accepted for publication Mar. 17, 2005; published online Aug. 1, 2005.

1 Introduction

According to recent estimates by the American Cancer Society, over one million new cases of cancer will be diagnosed each year.¹ One in every two men and one in every three women will be diagnosed with cancer at some point during his or her lifetime. Early detection of premalignant cellular aberrations in tissue has the potential to increase patient survival and recovery rates. However, many of the currently available cancer screening techniques, including physical biopsy and histopathology, are physically invasive in nature and require extensive training to yield reliable results. Therefore, more noninvasive, cost-effective, and quantitative methods are needed to identify precancerous lesions and improve the quality of care.

Optical diagnostics is a potentially more effective technique for early cancer detection. Since nearly 85% of all cancers originate in the epithelium,^{2,3} cellular dysplastic aberrations in the epithelial tissue are important indicators of precancers. Intraepithelial dysplasia can be characterized by increased nuclear size, increased nuclear-to-cytoplasmic ratio, hyperchromasia, and pleomorphism.^{2,3} The morphological features of intraepithelial dysplasia can potentially be as-

sessed through elastic-scattering (reflectance) spectroscopy, which yields information about the sizes and distributions of scatterers imbedded in tissue (e.g., nuclei and intracellular organelles) in a minimally invasive manner.⁴⁻⁹ The use of reflectance spectroscopy for precancer detection has been studied for numerous organ sites.^{7,10-14} Although the diagnostic accuracy of optical techniques has been extensively investigated in many preliminary studies,¹⁵⁻²⁰ there is a compelling need to refine the tissue-depth selectivity of both reflectance- and fluorescence-based spectroscopic techniques to enhance their diagnostic performances for probing tissue morphology and biochemistry more specifically.

Microscopic changes in cellular and nuclear morphology yield distinctive reflectance spectra that in principle may be used to ascertain tissue physiological status.²¹⁻²⁸ While tissue morphology and biochemistry in the epithelium can be effectively assessed by optical spectroscopy, only a small amount of the light incident on the tissue is backscattered by nuclei and other subcellular scatterers; the rest would tend to penetrate greater distances into the tissue.²⁹ These diffusely scattered photons are randomized by multiple scattering, and the background reflectance can potentially mask the reflectance from the epithelium. Localized tissue interrogation may improve the diagnostic sensitivity to intraepithelial lesions by

Address all correspondence to Rebekah Drezek, Bioengineering, Rice University, PO Box 1892, MS-142 — 6100 Main Street, Houston, TX 77251-1892. Tel: 713-348-3011. Fax: 713-348-5877. E-mail: drezek@rice.edu

methods that predominantly sample light traveling through controlled depths within the epithelium.

One proposed approach to separate the singly and multiply scattered light utilizes the polarization properties of light scattered in tissue.^{9,30-33} Polarized reflectance spectroscopy can be used to isolate the epithelial scattering signal from the bulk measurement. Studies of polarized reflectance spectroscopy have indicated that the diffusely scattering background and hemoglobin absorption can be significantly reduced by illuminating tissue with polarized light and detecting the reflectance at the same polarization as the source. Since light polarization is randomized by multiple scattering events, the reflectance component that maintains the original polarization mainly originates from the superficial epithelial layer, while the randomly polarized component is mainly from the deeper layers.^{9,30-35}

Another potentially effective means to facilitate the detection of reflectance signals from specific depths uses light delivery-and-collection geometries to selectively collect either the superficially or deeply scattered light from bulk reflectance. The primary geometrical parameters of a fiber optic probe for light delivery and collection include source-detector separation distances (SDSD),³⁶⁻³⁸ fiber aperture sizes,³⁹⁻⁴³ fiber numerical apertures,^{39,41,44} and spaces between the distal tip of a fiber probe and tissue surface.^{39,40,45} Increasing the source-detector separation distance yields an increase in the penetration depths of collected photons, and the multiply scattered background signal can be effectively measured by using a sufficient SDSD. Larsson et al.^{46,47} have also demonstrated that the same principle of SDSD can be applied to manipulate the probing capability of laser Doppler flowmetry, a variation of reflectance-based diagnostic techniques for microcirculatory blood flow in tissue. On the other hand, using a single-fiber probe, for which the SDSD value is zero, enables greater sensitivity to the superficially scattered light.

Another parameter that potentially affects the spatial selectivity of a fiber probe is the overlapping volume between the illumination and collection fibers. Several studies have discovered that the location and expanse of this overlapping volume seemingly influence the spatial selectivity of reflectance and fluorescence signals.⁴⁸⁻⁵⁰ It is possible to manipulate the depth selection of a fiber optic probe by confining the overlapping region to a specific tissue area of interest, and this can be done effectively by adjusting the angular orientation of the illumination or collection fibers. Skala et al.,⁴⁹ in their Monte Carlo study, showed that the fluorescence sensitivity to the epithelial layer dramatically improved from roughly 15 to 72% at a source-detector separation of $200\ \mu\text{m}$ when the *illumination* angle measured from the normal to tissue surface increased from 0 (orthogonal) to 45 deg. Since the spatial sensitivity of fluorescence emission depends greatly on the locations of fluorophore excitation, it is understandable that oblique illumination angles will enable more excited superficial fluorophores, and subsequently greater superficial fluorescence will be detected. A similar principle may be applied to reflectance spectroscopy, because more photons will propagate in the proximity of tissue surface when the illumination angles are high and the trajectories of photon injection are closer to the tissue surface.

In this study, we maintained the conventional orthogonal illumination and investigated the effects of variable detection

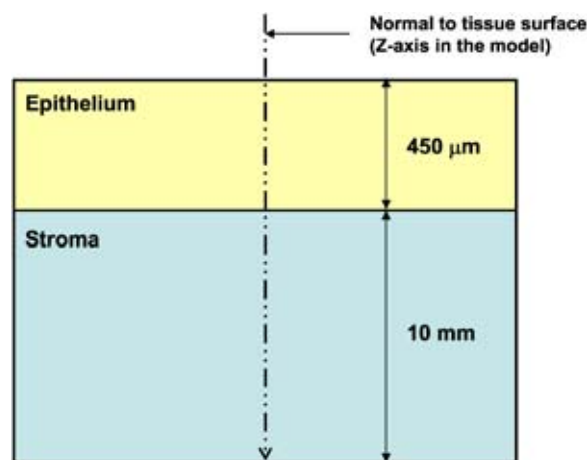


Fig. 1 Profile view of layered tissue structure.

orientation in relation to the tissue surface. In addition to controlling the overlaps between illumination and collection fibers, the angular orientation of collection fibers also determines the detectable exit angles for photons re-emitted at the tissue surface. We used Monte Carlo simulations to assess the spatial content of reflectance signals that were captured at various detection angles, along with additional geometric parameters such as source-detector separation distances, numerical apertures, and index matching at the tissue-fiber interface. Numerical apertures, which determine the half angles of fiber collection cones, affect the expanse of fiber overlap and range of detectable photon exit angles. Potential index mismatch across the tissue-fiber interface may also affect the angular orientation of fiber optical axes due to refraction. Hence, these geometric parameters may intricately affect the overall performance of a fiber probe, and their individual effects to the depth-resolved reflectance sampling is discussed. The objective of this study is to analyze and elucidate the significance of fiber geometries for the purpose of providing a quantitative assessment about geometric configurations of fiber probes for reflectance spectroscopy.

2 Methods

2.1 Tissue Model Geometry and Optical Properties

A two-layer cylindrical tissue model was constructed to represent human cervical epithelial tissue. In system coordinates, the longitudinal axis of the cylinder was in the Z direction, and the tissue surface occupied the x - y plane. The thickness of the epithelium was set at $450\ \mu\text{m}$ to approximate the average thickness of human cervical epithelium.⁵¹ The stroma was modeled as a cylindrical slab with a 10-mm thickness, representative of a semi-infinite tissue layer underneath the epithelium. The cylindrical model was set wide enough (10-mm radius) to encompass all possible photon paths to ensure the comprehensiveness of this simulation. The profile of this layered tissue structure can be found in Fig. 1. The optical properties of human cervical epithelial tissue (Table 1) were based on the literature values reported by Drezek et al.⁵² with additional references among other previously accepted

Table 1 Tissue optical properties implemented in this simulation model.

| Tissue layer | Tissue optical properties $\lambda=500$ nm | | | |
|--------------|--|------------------------------|--------------------------|------|
| | μ_a [mm^{-1}] | μ_s [mm^{-1}] | g [mm^{-1}] | n |
| Epithelium | 0.2 | 8.3 | 0.94 | 1.37 |
| Stroma | 0.3 | 22.5 | 0.89 | 1.37 |

values.^{7,41,49,53–56} Tissue optical properties corresponding to a wavelength of 500 nm were implemented in the simulation models.

2.2 Fiber-Probe Geometry

We investigated three specific fiber-probe configurations: a single fiber for illumination and collection, multiple collection fibers orthogonal to the tissue surface (parallel to the illumi-

nation), and multiple collection fibers angled with respect to the illumination axis. The illumination fibers were invariantly oriented perpendicularly to the tissue surface for all proposed probe geometries, and only the position and orientation of collection fibers were changed in this study. Schematic illustrations of the proposed fiber-probe configurations can be found in Fig. 2. Fiber diameters were set at $100\ \mu\text{m}$ for all fiber optics simulated in this study.

The single illumination-collection fiber was positioned at the center of the cylindrical tissue model. The source-detector separation distance (SDSD) is defined as zero for the single fiber, since SDSD measures the center-to-center distance between the illumination and collection fibers. The single-fiber probe has a complete overlap between its illumination and collection cone and is sensitive to direct backscattering from superficial tissue depths.^{38–41,56} To facilitate comparisons between various probe designs, the single-fiber geometry is designated as the reference in the evaluation of other probe geometries.

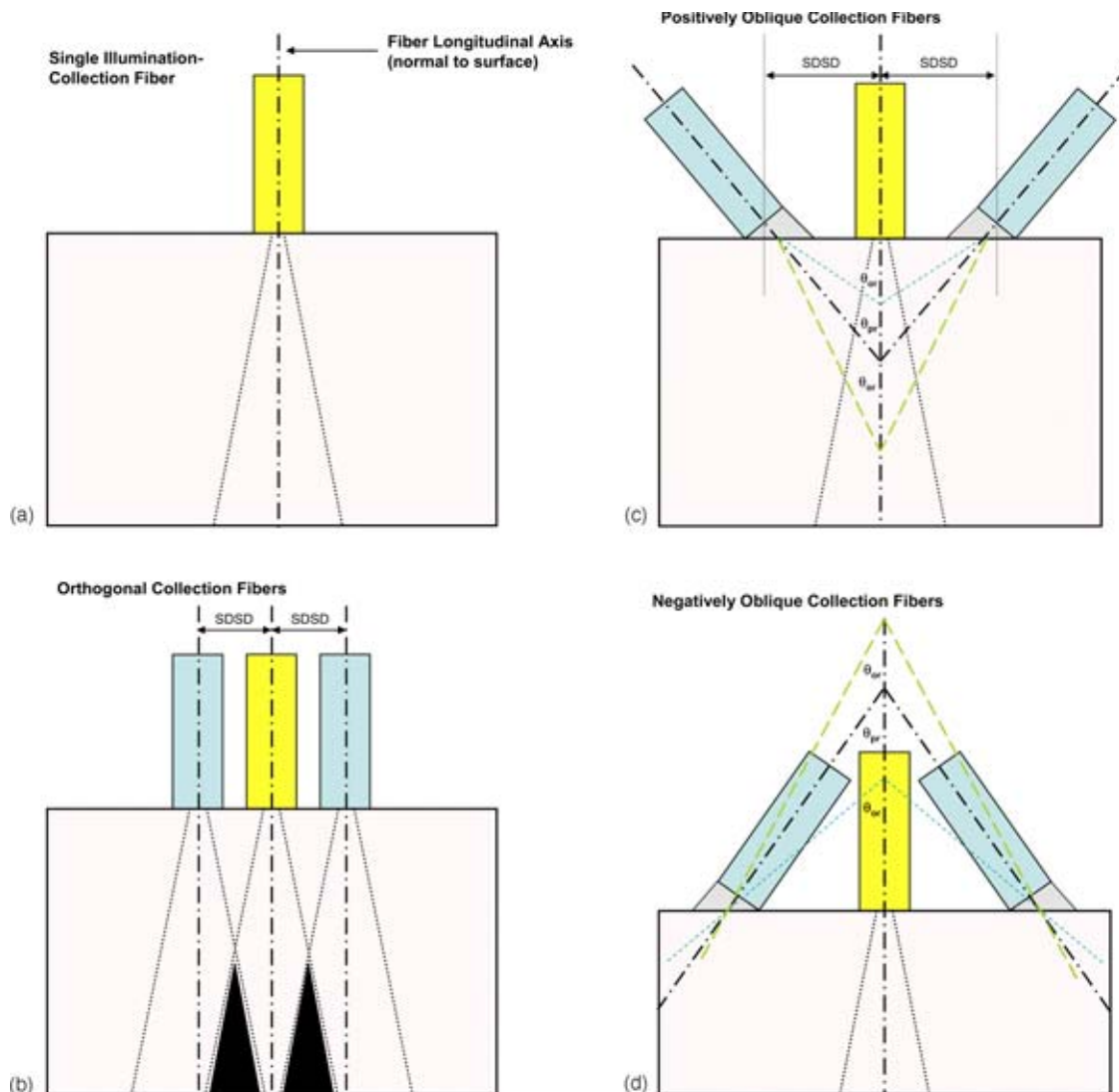


Fig. 2 (a) Schematic of the single illumination-collection fiber geometry. (b) Orthogonal fiber geometry. (c) Positively oblique fiber geometry. (d) Negatively oblique fiber geometry.

In the two other cases where separate collection fibers were used, the collection fibers were positioned at pre-designated SDS (150, 300, 500, and 800 μm) from the illumination axis. 3-D solid fiber models were inserted into the simulation program to achieve realistic spatial configurations of optical fibers in fiber probes. The collection fibers were evenly spaced and positioned concentrically about the illumination axis at each SDS, and each fiber was individually modeled as a solid 3-D object. Only photons reaching the distal facets of the collection fibers were admitted according to the specification of fiber numerical aperture: photons that came in contact with the opaque components of the fiber probes, including the exterior wall of the fiber optics, were nullified and excluded from the simulations and results. It should be noted that the concentrically arranged collection fibers at their respective SDS effectively formed an imaginary collection circle whose circumference perpendicularly intersected the longitudinal axes of the collection fibers. Because the circumference of the imaginary collection circle was directly proportional to its radius (i.e., SDS), the number of collection fibers on each circle also increased with respect to the values of SDS: the numbers of collection fibers positioned at their corresponding SDS—150, 300, 500, and 800 μm —were 9, 18, 31, and 50. It must be stressed that fibers on the same collection circle were geometrically equivalent due to the symmetry about the illumination axis. If the illumination angle were to deviate from its orthogonal orientation with respect to tissue surface, this symmetry and the collection-fiber equivalency would be no longer valid. The rationale of installing full circles of collection fibers was twofold. First, multiple collection fibers were implemented in the models to increase the efficiency of Monte Carlo simulation: increasing the detection area (i.e., cross-sectional area of a fiber multiplied by the number of fibers) shortened the time necessary to achieve convergence in the simulation process. Second, the signal collection efficiency of realistic fiber probes was usually maximized by adopting the same circular arrangement of multiple collection fibers around the illumination axis, thus our models would emulate circularly arranged probes of similar geometries to achieve more representative reflectance readings as with realistic probes.

The geometric configurations and arrangements of the oblique collection fibers were identical to their orthogonal counterparts as described before, with the only exception being their relative angular orientation with respect to the illumination axis. The physical axes of the collection fibers were rotated about the tissue surface to achieve an angle between the illumination and collection axes. We defined fiber facets rotating toward the illumination axis to be the positive angles [Fig. 2(c)] and negative angles as fiber facets rotating away from the illumination axis [Fig. 2(d)]. Angles of rotation implemented were 10, 20, 40, 60, 75, -10 , and -25 deg.

When oriented perpendicularly to a media, the physical and optical axes of fiber optics are equivalent to each other. When implemented with an angle, the optical axes of the oblique fibers may deflect from their physical axes due to refraction. Therefore, the optical rotational angles may not be the same as the physical rotational angles specified previously. In Fig. 2, the physical rotational angle (θ_{pr}) is defined as the angle between the physical axes of the illumination and

Table 2 Values of physical and optical rotational angles of fibers in tissue with different index-matching media calculated by Snell's law.

| Fiber type | Physical rotation (θ_{pr}) | Optical rotation (θ_{or}) in tissue ($n=1.37$) index matched by | |
|---------------------|-------------------------------------|--|-------------------|
| | | Water ($n=1.33$) | Glass ($n=1.5$) |
| Illumination | | | |
| orthogonal | 0 deg | 0 deg | 0 deg |
| Collection | | | |
| orthogonal | 0 | 0 | 0 |
| oblique | 10 | 9.71 | 11.0 |
| (in deg) | 20 | 19.4 | 22.0 |
| | 40 | 38.6 | 44.7 |
| | 60 | 57.2 | 71.5 |
| | 75 | 69.7 | N/A |
| | -10 | -9.71 | -11.0 |
| | -25 | -24.2 | -27.6 |

collection fibers: the optical rotational angle (θ_{or}) is the angle between the optical axes of the two. The location and magnitude of θ_{or} relative to θ_{pr} are dependent on the refractive index mismatch across the tissue-fiber boundary: the long-dashed line represents a hypothetical optical axis for the situation in which the external refractive index is smaller than that of the tissue, and the short-dashed line represents the opposite situation. The values of θ_{pr} and their corresponding θ_{or} used in this study are enumerated in Table 2. Since $\theta_{pr} = 75$ deg exceeds the critical angle specified by Snell's law for the glass-to-tissue interface, θ_{or} is not available for the corresponding entry in Table 2.

Index-matching materials were used to fill the gap between the distal end of fiber probes and tissue surface. Water ($n=1.33$) and glass ($n=1.5$) were the two materials proposed in the simulation models. Water is one of the most widely used index-matching fluids and a good representation of realistic index-matching schemes in experimental and clinical setups. A glass optical window is a commonly used component integrated into fiber probes to provide better index matching. A glass optical window can be fabricated with specific dimensions and shapes to be fitted in probes of different geometries. For the oblique fiber probes as illustrated in Fig. 2, glass optic wedges can be affixed onto the distal ends of fiber optics in place of air or water.

Numerical aperture (NA) specifies the half angle (HA) of fiber optics via the following relationship:

$$\text{HA} = \sin^{-1}\left(\frac{\text{NA}}{n_m}\right) = \sin^{-1}(\text{NA}_{\text{eff}}), \quad (1)$$

where NA is the nominal numerical aperture measured in vacuum, n_m is the refractive index of the surrounding me-

Table 3 Effective NA and half angles with respect to different ambient media. Values in parentheses are degrees of angle.

| Nominal NA (half angle) | Effective NA (half angle) | | |
|-------------------------|---------------------------|-----------------------|----------------------|
| | In tissue ($n=1.37$) | In water ($n=1.33$) | In glass ($n=1.5$) |
| 0.22 (12.7) | 0.16 (9.24) | 0.17 (9.52) | 0.15 (8.43) |
| 0.28 (16.3) | 0.20 (11.8) | 0.21 (12.2) | 0.19 (10.8) |
| 0.34 (19.9) | 0.25 (14.4) | 0.26 (14.8) | 0.23 (13.1) |
| 0.48 (28.7) | 0.35 (20.5) | 0.36 (21.2) | 0.32 (18.7) |
| 0.65 (40.5) | 0.47 (28.3) | 0.49 (29.3) | 0.43 (25.7) |
| 1.00 (90.0) | 0.73 (46.9) | 0.75 (48.8) | 0.67 (41.8) |

dium, and NA_{eff} is the effective numerical aperture measured in the medium. Six sets of nominal NA values (0.22, 0.28, 0.34, 0.48, 0.65, and 1) were implemented in this study to compare the reflectance data due to different numerical apertures. Although optical fibers have limited nominal numerical apertures, we decided to simulate the full range of NA values to delineate the complete effects of fiber numerical apertures. Table 3 lists the nominal and effective NA for fibers immersed in or in contact with different media used in this study. The actual numerical apertures incorporated in our simulations are based on the values of the effective NA.

2.3 Ray Tracing Setup and TracePro® Simulation

TracePro® by Lambda Research (Littleton, Massachusetts) was the ray tracing program used for the theoretical simulations. TracePro® utilizes the well-established Monte Carlo solid modeling method to simulate photon interactions with tissue. The human interface of TracePro® is similar to that of CAD, and allows users to graphically designate the geometric details of fibers and tissue models. Details about Monte Carlo modeling can be found in many literary texts.^{57–62} MATLAB® version 6.5 by Mathworks, Incorporated was used for postsimulation data processing.

Illumination photons were guided through a perpendicularly oriented illumination fiber at the center of the tissue surface. The nominal numerical aperture for illumination was 0.22. An evaluation of simulation convergence was conducted prior to the simulation trials. We ran ten groups of trial simulations with increasing numbers of incident rays (100 thousands to 1 million in increments of 100 thousands, 10 runs per group) and calculated the detected reflectance convergence. At the ray count of 100 thousands, the standard error of the mean sampled reflectance was less than 2.7%, and this value was further reduced to 0.78% when the ray count reached 1 million. Therefore, 1 million incident photons were sufficient enough to provide the desired data convergence, and 10 million incident photons were used for simulations to have extra data sampling.

2.4 Analysis of the Simulation Data

The detected photons were inventoried according to their weight, path lengths, coordinates of scattering, and directional

vectors between scattering events. From these quantities, we can calculate the maximal penetration depth, mean penetration depth, cumulative path length in tissue, sensitivity to each tissue layer, and exit angle of individual photons.

Unlike fluorescence emission, which has fixed fluorophores at specific tissue depths, it is more difficult to clearly characterize the depths of photon penetration in tissue for reflectance rays. We use multiple parameters to quantify the depths of photon migration in our models. The maximal penetration depth (Z_{max}) of each detected photon is defined as the greatest displacement of photon propagation in tissue in the axial direction (Z axis) measured from the point of entry ($Z_0=0$). Although Z_{max} does not completely represent the spatial distribution of photons in tissue because it only quantifies photon movements in the axial direction and ignores the lateral movements of photons, the concept of Z_{max} is easily visualized and unambiguous. Better quantifying photon movements is the mean penetration depth \bar{Z} of each detected photon [Eq. (2)], which is calculated from the mean occupancy of level z by a photon. By the nomenclature of “occupancy of level z ,” we mean the fraction of time spent by a photon at depth z before reaching the collection fibers.^{63,64} \bar{Z} may be tangibly characterized as the weight of a photon’s probing range in tissue: a photon’s axial probing range is bounded by 0 (tissue surface) and Z_{max} (maximal penetration depth), and \bar{Z} represents the central location of this probing range in the axial direction. \bar{Z} may be expressed as the sum of tissue depths multiplied by the probability of a photon occupying particular depths during photon migration in tissue (from the point of entry to exit).

$$\bar{Z} = \int_{\text{entry}}^{\text{exit}} z \cdot p(z) dz. \quad (2)$$

Since Monte Carlo simulation treats photons as individual packets propagating along linear segments between scattering events, for a photon that scattered n times in tissue, Eq. (2) can be expressed as the summation of individual segments between scattering points p_i and p_{i+1} :

$$\bar{Z} = \sum_{i=0}^n \int_{p_i}^{p_{i+1}} z \cdot p(z) dz, \quad (3)$$

where i is the index marking the sequence of scattering ($i=0$ is the point of entry and $i=n+1$ is the point of exit). Along the transit from point p_i to p_{i+1} , the probability of a photon occupying each incremental interval on the segment is the ratio of the incremental path length dpl to the total path length (L):

$$p(z) dz|_{p_i}^{p_{i+1}} = \frac{dpl}{L} = \frac{dz \sec \theta_i}{L}. \quad (4)$$

The incremental path length dpl can be expressed as the product of dz and $\sec \theta_i$ by trigonometry, where θ_i is the angle between the Z axis and the directional vector of a photon moving from scattering point p_i to p_{i+1} . Substituting Eq. (4) into Eq. (3), we get:

$$\begin{aligned} \bar{Z} &= \sum_{i=0}^n \int_{Z_i}^{Z_{i+1}} z \cdot \frac{\sec \theta_i}{L} dz = \sum_{i=0}^n \frac{(Z_{i+1} + Z_i)}{2} \cdot \frac{(Z_{i+1} - Z_i) \sec \theta_i}{L} \\ &= \sum_{i=0}^n Z_{\text{mid}(i,i+1)} \cdot \frac{pl_{i,i+1}}{L}, \end{aligned} \quad (5)$$

where $Z_{\text{mid}(i,i+1)}$ and $pl_{i,i+1}$ are the midpoint in Z and distance between scattering points p_i and p_{i+1} , respectively. The value of \bar{Z} depends on the course of propagation of a photon in both axial and lateral directions, and the average ratio of \bar{Z} to Z_{max} ranges from 0.53 to 0.56 in our model. This result follows the prediction by Gandjbakhche et al. for tissue conditions as in our model.^{63,64} Note that the physical interpretation of \bar{Z} is not the same as Z_{max} ; for instance, for a photon with $Z_{\text{max}} = 600 \mu\text{m}$, which is well into the stromal region in our model, its corresponding \bar{Z} is roughly $320 \mu\text{m}$. This by no means signifies that the photon only probes to a depth of $320 \mu\text{m}$, which is well below the epithelial thickness of our model ($450 \mu\text{m}$). Instead, it denotes the center of a probing range that extends $600 \mu\text{m}$ from the tissue surface. The previous conversion ratio of 0.53 to 0.56 specific to our model may be used to relate the values of \bar{Z} and Z_{max} .

The sensitivities of individual photons to epithelium and stroma (S_{Ep} and S_{St} , respectively) are defined as the following:

$$S_{\text{Ep}} = \frac{\text{path length in epithelium}}{\text{total path length}} = \frac{pl_{\text{Ep}}}{L}, \quad (6)$$

$$S_{\text{St}} = \frac{\text{path length in stroma}}{\text{total path length}} = \frac{pl_{\text{St}}}{L} = 1 - S_{\text{Ep}}, \quad (7)$$

where pl_{Ep} and pl_{St} denote the respective path lengths traveled by a photon in the two layers.

Thus far, we have defined the maximal penetration depth, mean penetration depth, and layer sensitivities of individual photons. To characterize the probing capability and layer sensitivities of a fiber probe, we take the weighted average of these parameters with respect to each photon's contribution to

the total detected reflectance. Let the weight of a detected photon be f , the number of detected photons NP , and the total detected reflectance R , and then the expected values of mean probing depth and layer sensitivities of a fiber probe are:

$$\bar{Z}^{\text{Probe}} = \frac{\sum_{j=1}^{NP} f_j \cdot \bar{Z}_j}{\sum_{j=1}^{NP} f_j} = \frac{\sum_{j=1}^{NP} f_j \cdot \bar{Z}_j}{R}, \quad (8)$$

$$S_{\text{Ep}}^{\text{Probe}} = \frac{\sum_{j=1}^{NP} f_j \cdot S_{\text{Ep}j}}{\sum_{j=1}^{NP} f_j} = \frac{\sum_{j=1}^{NP} f_j \cdot S_{\text{Ep}j}}{R}, \quad (9)$$

$$S_{\text{St}}^{\text{Probe}} = \frac{\sum_{j=1}^{NP} f_j \cdot S_{\text{St}j}}{\sum_{j=1}^{NP} f_j} = \frac{\sum_{j=1}^{NP} f_j \cdot S_{\text{St}j}}{R} = 1 - S_{\text{Ep}}^{\text{Probe}}. \quad (10)$$

The total reflectance was normalized against the total illumination radiation injected into the tissue. Thus, in the following sections, we use "reflectance probability" (between 0 and 1) as the measure of signal strength harvested by various probe designs. To preserve the qualitative significance of this quantity, we refer to the reflectance probability as normalized reflectance in future sections.

3 Results

3.1 Depth-Resolved Reflectance for Variable Collection Angles

Figure 3 shows the normalized reflectance profiles binned over the mean penetration depths of photons measured every $10 \mu\text{m}$ with respect to various collection angles. Only 0, 20, 40, 60, and -25 deg are plotted for better readability of the graph. The fiber probes have a SDD of $300 \mu\text{m}$ and a nominal NA value of 0.34. Water is the selected index-matching material between the probes and tissue. Due to the double-layer structure of the tissue model, the appearance of double-peak reflectance distribution in Fig. 3 can be attributed to the discontinuity in tissue optical properties between the epithelial and stromal layers. Evaluation of Fig. 3 indicates that the mean penetration depth of photons decreases as the collection angle increases. The 0-deg fiber has a single reflectance peak at the mean penetration depth of approximately $320 \mu\text{m}$. As the collection angle increases, the peak of reflectance shifts leftward and the peak-to-width ratio increases. This indicates the penetration depths of the detected photons become more superficial and the spatial distributions of the photons become better defined. Figure 3 also suggests that the increasing collection angles enhance the signal strength of reflectance detection in the superficial region. As the collection angle increases in the positive direction, significant reflectance increase is seen for photons with mean penetration depths less than $200 \mu\text{m}$. By increasing the collection angle in the negative direction, we observe a decrease in the total reflectance and a shift into deeper depths. The spatial distribution of photons is less defined as the peak-to-width of the reflectance curve diminishes for the negative-angle fibers. Figure 4 includes the cumulative percentage distribution curves of the detected reflectance with respect to the mean penetration

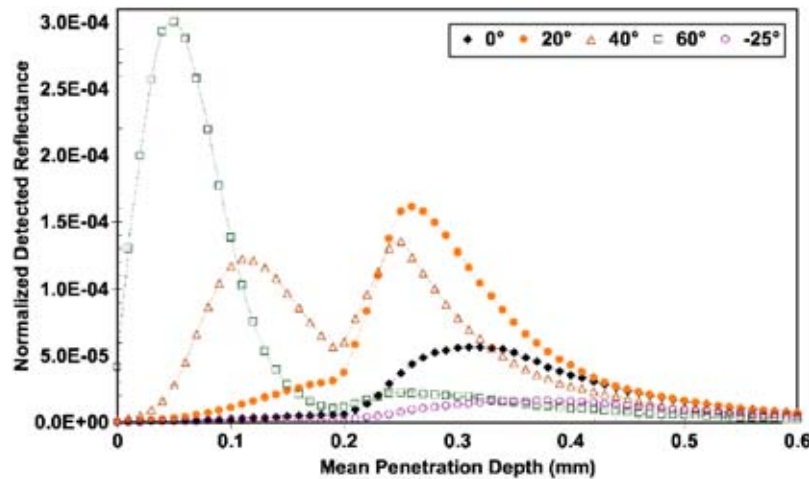


Fig. 3 Depth-resolved normalized reflectance measured at SDSD=300 μm .

depths, and it is clear that collection angles have dominant effects on the spatial distributions of sampled reflectance. For fibers with positive angles, significant portions of detected photons have shallow mean penetration depths in comparison to the normal fiber, whereas the negative-angle fibers push the distribution into deeper regions of the tissue and consequently may be more sensitive to the tissue characteristics of the bottom layers.

3.2 Depth-Resolved Reflectance for Variable Source-Detector Separation Distances

Figures 5(a)–5(d) display the percent reflectance distribution with respect to the photon's mean penetration depths by fiber probes with various SDSD and collection angles. The nominal numerical aperture of the fiber probes remains at 0.34 and is index matched by water. The x axis is divided into intervals of 10 μm , and the partial reflectance corresponding to each division is summed and weighted against the total reflectance detected by each fiber probe. The single-fiber geometry (0 μm 0 deg) was used as the reference to better facilitate contrast and comparison among the diagrams. As SDSD in-

creases, the weight of detected reflectance persistently shifts toward the greater end of the x axis, and this is observed for all collection angles. Collection angles have profound effects on the depth-resolved distribution of detected reflectance. The weight of early returning photons in the total reflectance rises with increasing collection angles, and this is manifested by the rise and leftward shift of the curves in Fig. 5. On the other hand, by implementing oblique fibers in the negative direction, deeper reflectance sampling was induced and accompanied by the diminishment of early returning photons. Diagrams in Fig. 5 have demonstrated the potential to control the probing depths and spatial sensitivities of fiber probes by manipulating geometric parameters such as SDSD and collection angles. Combinations of SDSD and collection angles can be utilized to achieve depth selectivity in reflectance sampling for various situations.

Figure 6(a) displays the magnitudes of reflectance detected per individual fiber placed at various SDSD. The detected reflectance is normalized to the illumination. Fiber nominal NA remains the same as in Fig. 5 (0.34) and is index matched by water. The single-fiber geometry, being positioned at the

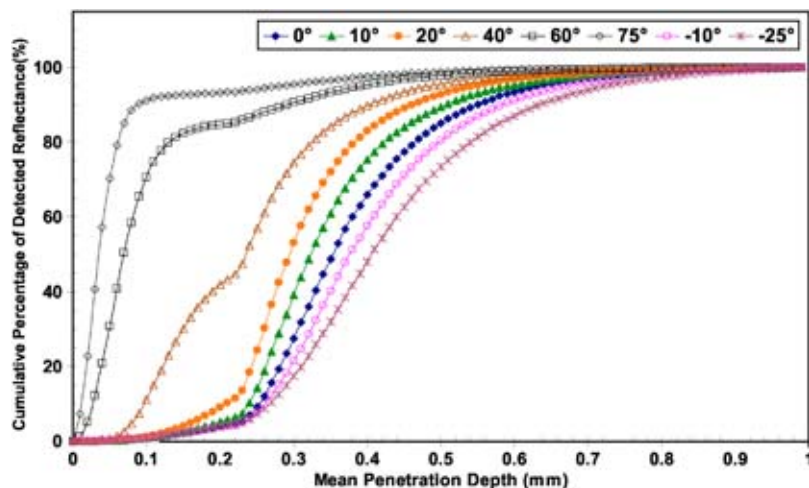


Fig. 4 Cumulative percentage distribution of reflectance measured at SDSD=300 μm .

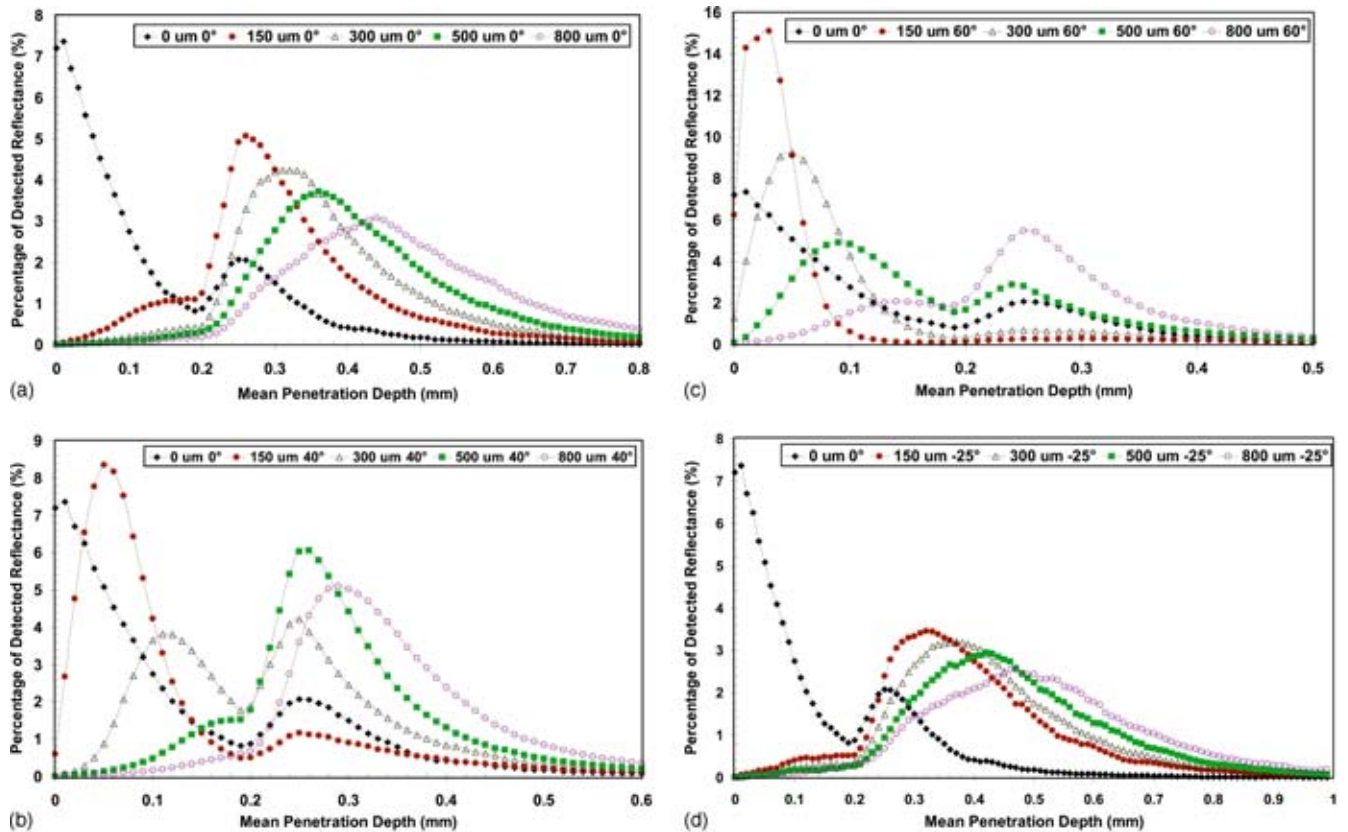


Fig. 5 Percent reflectance distribution measured at (a) 0, (b) 40, (c) 60, and (d) -25 deg.

point of illumination, has the strongest reflectance per fiber, while the magnitude of reflectance quickly recedes with increasing SDSD. We also observe a consistent increase in detected reflectance per fiber when the collection angle increases from 0 to 40 deg. We attribute the rise in reflectance to the increasing number of detected photons and the greater individual weights of these photons: the center of reflectance detection shifts toward superficial depths as the collection angle increases, and early returning photons have higher weights due to their shorter path lengths in tissue. For collection angles of 60 and 75 deg, the total number of detected photons decreases as the collection angle continues to rise. This is primarily due to the much limited tissue sampling volume and lower probability for photons exiting the tissue surface with extremely steep trajectories. Although the detected reflectance per individual fiber diminishes as SDSD increases, multiple collection fibers can be implemented in a circular configuration as in this study to improve the detection efficiency of fiber probes. This is the advantage of implementing multiple fibers in a fiber probe with SDSD greater than 0. Figure 6(b) displays the total detected reflectance by each probe unit, and the values displayed are multiples of those shown Fig. 6(a), contingent on the number of collection fibers implemented in these probes. Note that the difference in total reflectance per probe among different SDSD configurations is greatest at collection angles of 60 and 75 deg.

3.3 Depth-Resolved Reflectance for Variable Fiber Numerical Apertures

In Fig. 7, the effects of numerical apertures on fiber expected probing depths are displayed and compared. The x axis lists

the six nominal NA of the collection fibers tested in this study, and the y axis represents the expected probing depth of fiber probes. With water as the index-matching material, the effective NA of the fiber probes increases from 0.17 to 0.75. Correspondingly, the effective half angles of the fiber probes vary from 9.52 to 48.8 deg (Table 3). Evaluation of Fig. 7 shows that the effects of NA on the expected probing depth are subtle and contingent on the angles of collection fibers. For fibers with collection angles from 0 to 20 deg, the expected probing depths gradually decrease with respect to increasing NA values; a similar observation is made for the negative-angle collection fibers. The opposite is observed for fibers with collection angles from 40 to 75 deg, for which the expected probing depths become greater as the NA value increases.

3.4 Fiber Expected Probing Depths and Layer Sensitivities

As we have shown that both collection angles and SDSD have significant influences over the spatial distributions of detected photons in tissue, collection angles and SDSD are expected to have similar effects on the expected fiber probing depths and layer sensitivities. Having the nominal fiber NA=0.34 (index matched by water), Figs. 8(a) and 9(a) display the expected fiber probing depths and layer sensitivities under various fiber configurations, respectively. The expected probing depth of a fiber probe decreases as the collection angle increases in the positive direction, while extended probing depths can be observed for negative collection angles. A trend in the sensitivities to the epithelial layer of a fiber probe, which echoes the

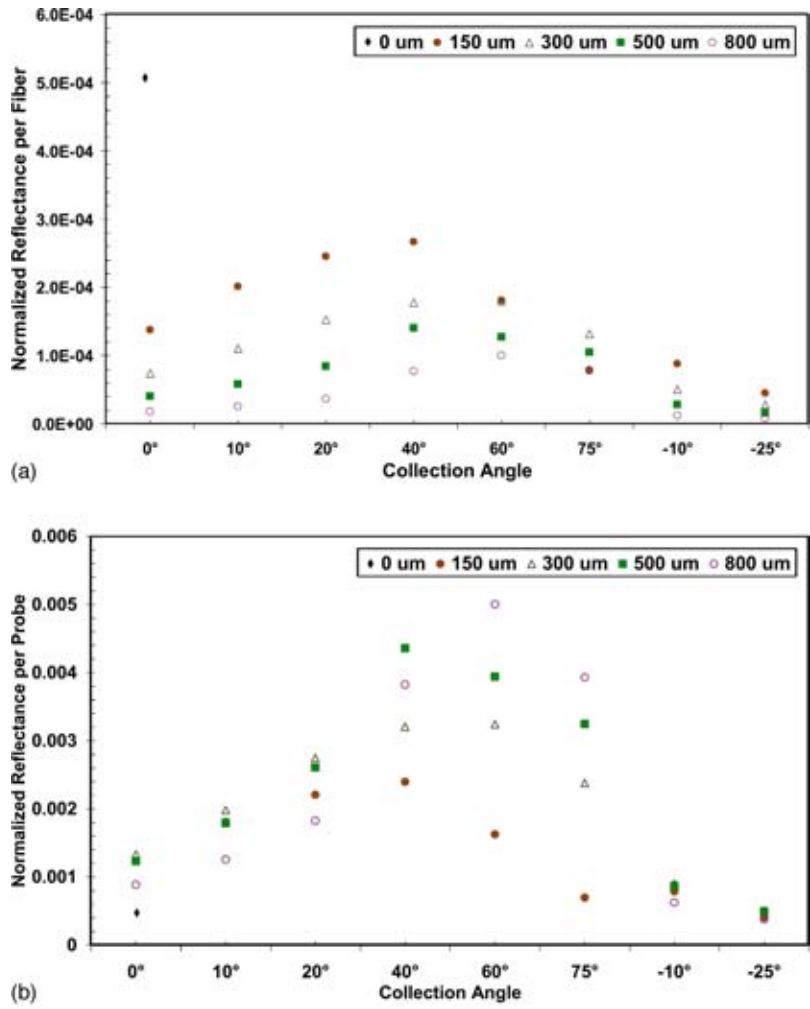


Fig. 6 (a) Normalized reflectance per fiber at various collection angles and SDSD, and (b) normalized reflectance per probe unit at various collection angles and SDSD.

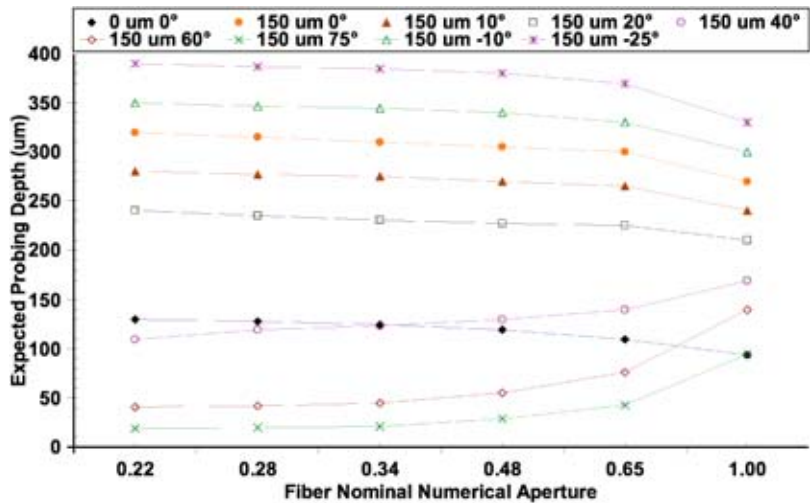


Fig. 7 Effects of fiber NA on expected probing depths of fiber probes (index-matched by water).

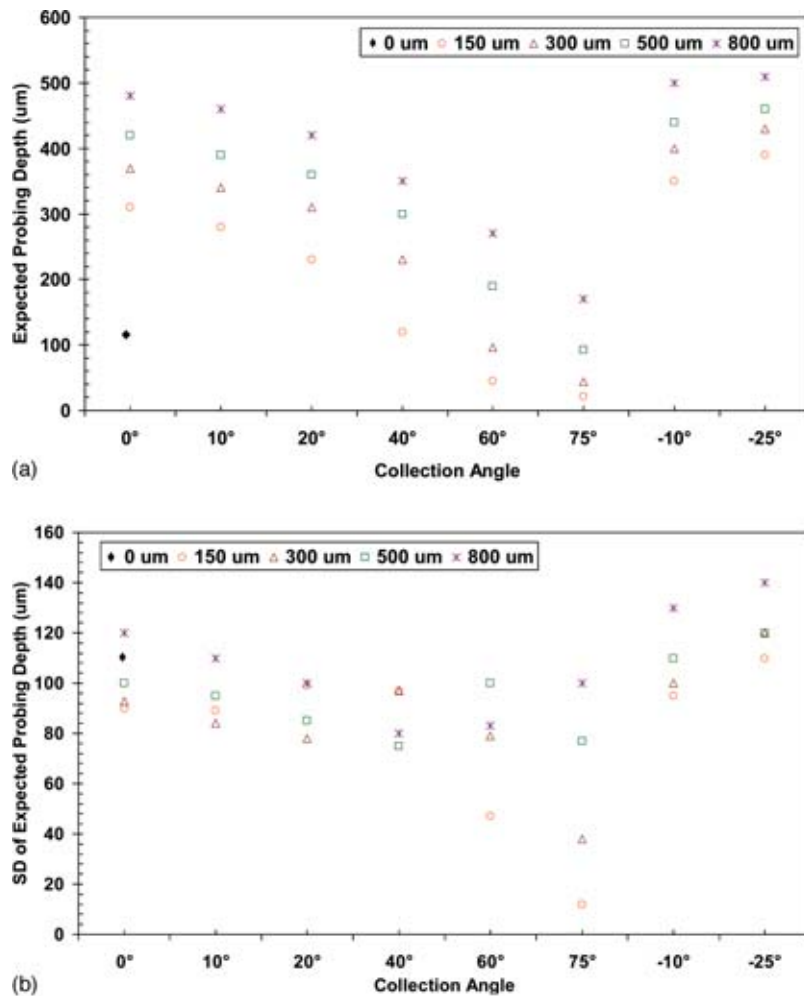


Fig. 8 (a) Effects of collection angles and SDSD on expected probing depths of fiber probes. (b) Standard deviations of expected probing depths for probes with various collection angles and SDSD.

shifts in expected fiber probing depths in Fig. 8(a), can be observed in Fig. 9(a). Figures 8(b) and 9(b) are the respective standard deviations corresponding to the expected values shown in Figs. 8(a) and 9(a). The standard deviations of the expected probing depths and layer sensitivities generally decrease with increasing collection angles but increase with greater source-detector separation.⁶⁵ An increase in standard deviation indicates that the sampled reflectance is less spatially specific and comprises photons from a broader spread of tissue depths. The opposite effects of SDSD and collection angles create a transition in the expected probing depths of fiber probes, and when both effects are equally dominant, the expected variance would likely increase. For example, Fig. 3 shows the reflectance profiles with respect to photon's mean penetration depths in tissue for SDSD=300 μm with various collection angles. At 40 deg, there are two peaks of equal height at the mean penetration depths of 110 and 260 μm, and the observed standard deviation for SDSD=300 μm is the greatest at this angle. At either 20 or 60 deg, the distributions of sampled reflectance are more definitive, and consequently we may observe a decrease in the standard deviations of the expected probing depths at these two collection angles. The opposite effects of SDSD and collection angles may ex-

plain the sudden increases in the standard deviations of the expected probing depths at (SDSD, angle) = (150 μm, 20 deg), (300 μm, 40 deg), (500 μm, 60 deg) and (800 μm, 75 deg) in Fig. 8(b). To demonstrate the trend with respect to the collection angles in numerical details, the expected probing depths and sensitivities to the epithelial layer for SDSD=0 and 300 μm are listed in Tables 4 and 5, in which their respective standard deviations are enclosed in parentheses.

Another informative metric used to describe the probing capabilities of fiber probes is the locations of percentiles of depth-resolved reflectance, which express the spatial distribution and center of gravity of depth-resolved reflectance. Combined with the expected probing depths, we may obtain more information in regard to the range of photon mean penetration depths in tissue. Figure 10 plots the mean penetration depths of photons, at which the 10th, 50th (median), and 80th percentiles of reflectance were recorded at a SDSD of 300 μm. The nominal numerical aperture of the fiber probes is 0.34 and water is the index-matching material. The downward movements of 10th, 50th, and 80th percentiles markedly show that positively oblique fibers enhance the importance of early returning photons, and the vertical spacing between the per-

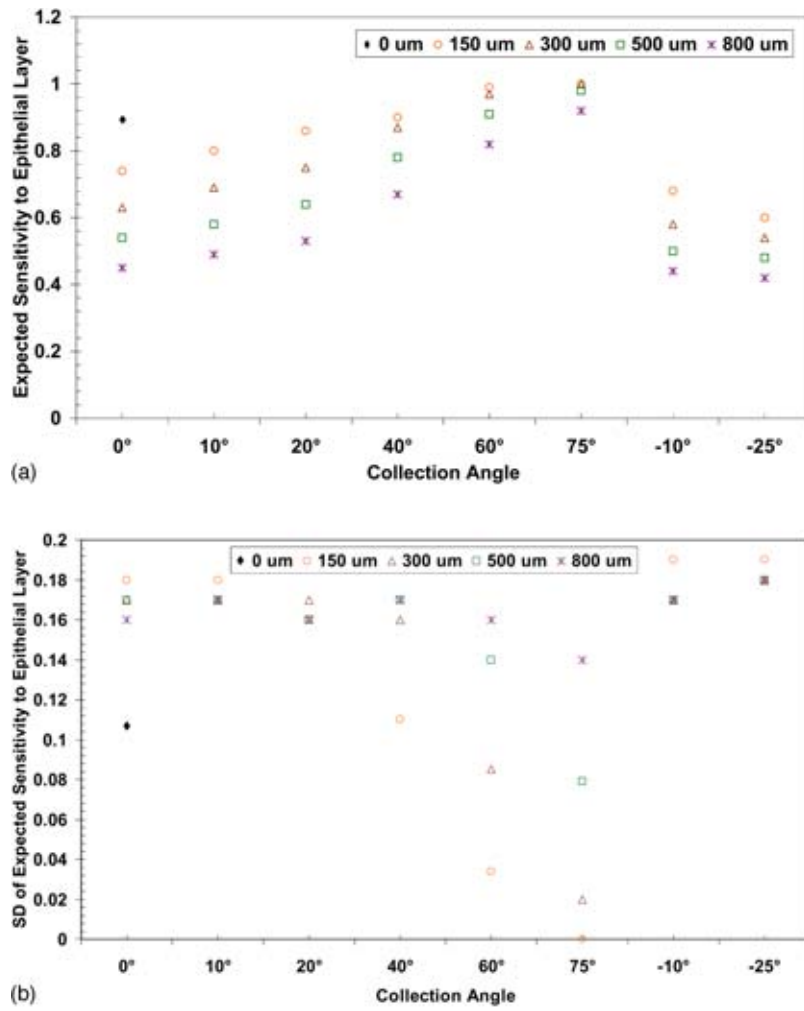


Fig. 9 (a) Effects of collection angles and SDSD on expected sensitivities to epithelial layer of fiber probes. (b) Standard deviations of expected sensitivities to epithelial layer for probes with various collection angles and SDSD.

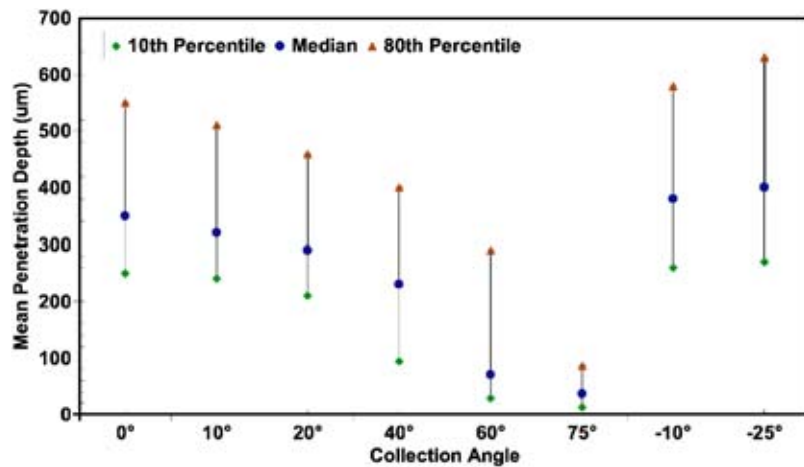


Fig. 10 The 10th, 50th (median), and 80th percentile of depth-resolved reflectance measured at various collection angles (SDSD=300 μm).

Table 4 Expected probing depth (and standard deviation) of fiber probes with respect to fiber geometry and index-matching conditions.

| Index match → Fiber NA → | Water ($n=1.33$) | | | | | | | Glass ($n=1.5$) | | | | | |
|--|--------------------|----------|----------|----------|----------|----------|----------|-------------------|----------|----------|----------|----------|----------|
| | 0.22 | 0.28 | 0.34 | 0.48 | 0.65 | 1.0 | 0.22 | 0.28 | 0.34 | 0.48 | 0.65 | 1.0 | |
| SDSD=0 μm SDSD=300 μm | 0 deg | 130(110) | 130(110) | 130(110) | 120(110) | 110(110) | 94(110) | 130(110) | 130(110) | 130(110) | 120(110) | 110(120) | 92(110) |
| | 0 deg | 370(92) | 370(92) | 370(93) | 370(93) | 360(94) | 340(110) | 370(94) | 370(94) | 370(94) | 370(94) | 360(95) | 340(110) |
| | 10 deg | 350(83) | 340(83) | 340(84) | 340(86) | 330(92) | 320(110) | 340(82) | 340(83) | 340(84) | 330(86) | 330(93) | 310(110) |
| | 20 deg | 310(73) | 310(75) | 310(78) | 310(85) | 310(96) | 290(120) | 300(72) | 300(75) | 300(78) | 300(87) | 300(99) | 280(130) |
| | 40 deg | 230(91) | 230(94) | 230(97) | 230(110) | 230(120) | 240(140) | 190(95) | 190(98) | 190(100) | 200(110) | 200(120) | 240(130) |
| | 60 deg | 88(67) | 91(73) | 96(79) | 110(97) | 140(120) | 200(130) | 41(24) | 48(36) | 57(47) | 80(73) | 110(100) | 190(130) |
| | 75 deg | 34(20) | 38(29) | 44(38) | 63(64) | 92(92) | 160(130) | N/A | 11(5.4) | 17(8.3) | 30(16) | 53(49) | 120(110) |
| | -10 deg | 400(100) | 400(100) | 400(100) | 390(100) | 380(100) | 350(100) | 400(100) | 400(100) | 400(100) | 390(100) | 380(100) | 360(100) |
| | -25 deg | 430(120) | 430(120) | 430(120) | 420(110) | 410(110) | 380(110) | 430(120) | 430(120) | 430(120) | 420(110) | 420(110) | 390(110) |

Table 5 Expected sensitivity to epithelial layer (and standard deviation) of fiber probes with respect to fiber geometry and index-matching conditions. For entries with expected epithelial sensitivities of 1, the standard deviation shown in the parentheses denotes deviation in the minus direction.

| Index match → Fiber NA → | Water ($n=1.33$) | | | | | | | Glass ($n=1.5$) | | | | | |
|--|--------------------|-------------|-------------|-------------|-------------|------------|------------|-------------------|------------|-------------|-------------|-------------|------------|
| | 0.22 | 0.28 | 0.34 | 0.48 | 0.65 | 1.0 | 0.22 | 0.28 | 0.34 | 0.48 | 0.65 | 1.0 | |
| SDSD=0 μm SDSD=300 μm | 0 deg | 0.95(0.11) | 0.94(0.11) | 0.94(0.11) | 0.94(0.12) | 0.94(0.12) | 0.95(0.12) | 0.94(0.11) | 0.94(0.12) | 0.94(0.12) | 0.94(0.12) | 0.94(0.12) | 0.95(0.12) |
| | 0 deg | 0.62(0.17) | 0.62(0.17) | 0.63(0.17) | 0.64(0.18) | 0.66(0.19) | 0.70(0.20) | 0.62(0.17) | 0.62(0.17) | 0.63(0.18) | 0.64(0.18) | 0.66(0.19) | 0.70(0.20) |
| | 10 deg | 0.68(0.17) | 0.68(0.17) | 0.69(0.17) | 0.70(0.18) | 0.71(0.19) | 0.73(0.21) | 0.69(0.17) | 0.69(0.17) | 0.70(0.17) | 0.70(0.18) | 0.71(0.19) | 0.73(0.21) |
| | 20 deg | 0.75(0.17) | 0.75(0.17) | 0.75(0.17) | 0.75(0.18) | 0.75(0.19) | 0.76(0.21) | 0.77(0.16) | 0.77(0.17) | 0.77(0.17) | 0.77(0.18) | 0.76(0.19) | 0.77(0.21) |
| | 40 deg | 0.88(0.16) | 0.88(0.16) | 0.87(0.16) | 0.86(0.17) | 0.84(0.18) | 0.82(0.20) | 0.92(0.14) | 0.91(0.15) | 0.91(0.15) | 0.90(0.16) | 0.88(0.17) | 0.83(0.20) |
| | 60 deg | 0.98(0.069) | 0.98(0.077) | 0.97(0.085) | 0.96(0.11) | 0.93(0.14) | 0.86(0.18) | 1.0(2.0e-3) | 1.0(0.018) | 0.99(0.033) | 0.98(0.072) | 0.96(0.11) | 0.89(0.17) |
| | 75 deg | 1.0(7e-5) | 1.0(9e-3) | 1.0(0.020) | 0.99(0.060) | 0.97(0.10) | 0.90(0.16) | N/A | 1.0(2e-16) | 1.0(2e-15) | 1.0(8e-15) | 0.99(0.036) | 0.94(0.13) |
| | -10 deg | 0.58(0.17) | 0.58(0.18) | 0.58(0.17) | 0.59(0.18) | 0.61(0.18) | 0.66(0.20) | 0.57(0.17) | 0.57(0.17) | 0.58(0.18) | 0.59(0.18) | 0.61(0.18) | 0.66(0.20) |
| | -25 deg | 0.53(0.18) | 0.54(0.18) | 0.54(0.18) | 0.55(0.18) | 0.56(0.18) | 0.61(0.19) | 0.53(0.19) | 0.53(0.19) | 0.53(0.18) | 0.54(0.18) | 0.55(0.18) | 0.60(0.19) |

Table 6 Mean penetration depths at which the 10th, 50th (median), and 80th percentile of depth-resolved reflectance were measured.

| Index match → Fiber NA → | Water (n= 1.33) | | | | | Glass (n= 1.5) | | | | | |
|-----------------------------|-----------------|-------------|-------------|-------------|-------------|----------------|-------------|-------------|-------------|-------------|-------------|
| | 0.22 | 0.28 | 0.34 | 0.48 | 1.0 | 0.22 | 0.28 | 0.34 | 0.48 | 0.65 | 1.0 |
| SDSD=0 μm SDSD=300 μm | 14-92-325 | 14-90-330 | 14-88-330 | 12-74-330 | 6-37-340 | 14-92-330 | 14-92-330 | 12-86-340 | 10-72-340 | 8-61-340 | 6-37-340 |
| 0 deg | 260-350-550 | 250-350-550 | 250-350-550 | 250-350-540 | 180-320-530 | 250-350-550 | 250-350-550 | 250-350-550 | 250-350-550 | 340-330-540 | 180-320-530 |
| 10 deg | 240-330-510 | 240-320-510 | 240-320-510 | 230-320-500 | 130-300-510 | 240-320-500 | 240-320-500 | 230-320-500 | 230-310-500 | 200-310-500 | 120-300-510 |
| 20 deg | 230-290-450 | 210-290-460 | 210-290-460 | 180-290-470 | 90-290-500 | 210-290-440 | 200-290-450 | 190-290-450 | 160-290-460 | 140-290-480 | 74-280-490 |
| 40 deg | 110-230-400 | 100-230-400 | 94-230-400 | 82-240-410 | 40-250-430 | 82-150-370 | 78-160-370 | 74-160-380 | 60-180-390 | 40-200-410 | 40-250-450 |
| 60 deg | 32-66-260 | 28-70-280 | 28-70-290 | 24-74-330 | 24-94-370 | 12-36-78 | 12-40-94 | 16-44-120 | 16-56-260 | 20-74-330 | 28-160-410 |
| 75 deg | 8-28-66 | 12-32-74 | 12-36-86 | 12-44-230 | 16-60-310 | N/A | 4-8-20 | 4-16-32 | 8-28-56 | 12-40-110 | 20-78-350 |
| -10 deg | 260-380-580 | 260-380-580 | 260-380-580 | 260-370-580 | 230-330-550 | 270-380-590 | 260-380-600 | 260-380-600 | 260-370-590 | 250-360-580 | 230-340-550 |
| -25 deg | 270-410-640 | 270-410-640 | 270-400-630 | 260-400-630 | 250-360-580 | 270-410-650 | 270-410-640 | 270-410-640 | 270-400-630 | 260-400-620 | 250-370-590 |

centile markers indicates the density of photon distribution with respect to the mean penetration depths. Table 6 lists the numerical values of the mean penetration depths at which the 10th, 50th (median), and 80th percentile of depth-resolved reflectance were measured at SDSD=0 and 300 μm.

3.5 Effects of Index Matching and Fiber Numerical Aperture

Transparent optical windows are used to improve the index-matching condition by eliminating the presence of air between fiber probes and tissue. Water is one of the most commonly used index-matching fluids with a refractive index of 1.33. Glass, whose refractive index is near 1.5, is a solid material commonly used in place of index-matching fluids. In this study, we investigated the effects of index matching on the depth selections of fiber probes, and the results are best observed in Table 4. We can observe a decrease in the expected probing depths of probes with positive-angle fibers when index matching is administered with glass. This effect is most prominent when fiber obliquity is high (i.e., ≥40 deg) and is almost nonexistent for orthogonally oriented fibers. Similar effects can be observed in Tables 5 and 6, where the layer sensitivities to epithelium and centers of gravity of depth-resolved reflectance are shifted accordingly. Due to refraction, no light was detected by the 75-deg fibers with a nominal NA of 0.22 when glass was implemented in the model.

Fiber numerical aperture imposes minor influences on the depth selection of fiber probes. Greater numerical apertures increase the half angles of fiber optics and result in more inclusive detections of light re-emitted from tissue. Figure 11 shows the normalized reflectance detected per fiber as nominal NA ranges from 0.22 to 1.0 when index matched by water. While increasing fiber NA from 0.22 to 0.34 does not significantly influence the expected probing depths of fiber probes, the magnitude of detected reflectance is doubled.

4 Discussion

From the data presented in previous sections, it is clear that the orientation of collection fibers has significant effects on the depth-wise distributions of sampled reflectance. Combined with source-detector separations, many depth-selective fiber probes can be created for various tissue types and situations. Studies of photon migrations^{39-42,64-68} have pointed out that photons detected at greater lateral distances from the source travel farther distances and depths in tissue. As a result, increasing SDSD can effectively extend the probing capability of fiber probes and increase the sensitivities to the bottom tissue structures. While the concept of source-detector separation is comparatively straightforward, the idea behind the effectiveness of fiber orientation is less conspicuous and has not been well discussed. This study has shown that varying the orientation of collection fibers at a given SDSD can effectively change the spatial characteristics of detected reflectance and thus manipulate the expected probing depths of fiber probes. Such effects are contingent on both the direction and obliquity of fiber orientation.

In addition to its depth selectivity, the angular orientation of a fiber optic probe affects the magnitude of detected reflectance. Taking the data shown in Figs. 6 and 11, with a given SDSD and fiber NA, reflectance detected at collection angle

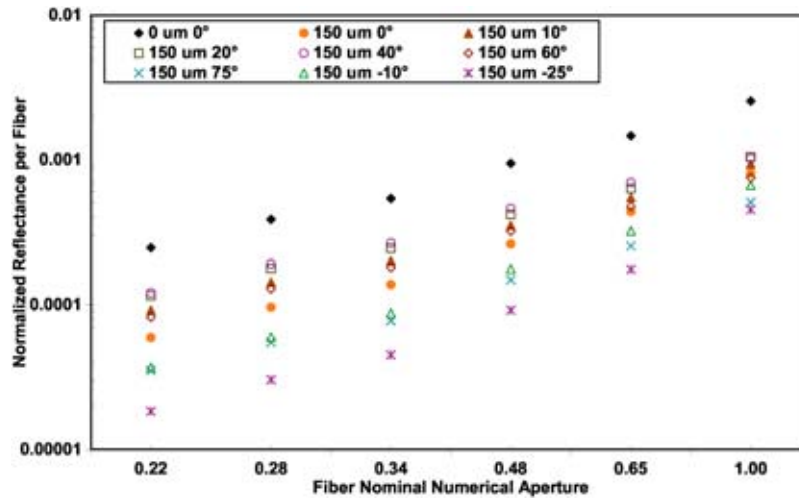


Fig. 11 Normalized reflectance per fiber detected with various fiber nominal numerical apertures (index matched by water).

of 40 deg is roughly twice as much as that sampled at the normal orientation. Such increase in reflectance can be explained by the angular distribution of re-emitted reflectance at the tissue-fiber interface. Not only more photons are recorded at exit angles near 40 deg, but the weights of individual photons also increase with increasing exit angles. This can be observed in Fig. 3, in which more early returning photons are detected at greater positive collection angles. These early returning photons endure less tissue absorption due to their limited path lengths. Consequently, we observe an increase in total reflectance detected at the 40-deg angle. The drop-off in total reflectance for probes at 60 and 75 deg can be attributed to the smaller probabilities of detecting rays at steep angles. The reason for the lower signal of the negative-angle fibers may be twofold. First, the negative-angle fibers tilt away from the illumination axis and consequently preclude the detection of photons re-emitted near the tissue center. Additionally, greater attenuations with increasing probing depths may impact the photonic weight trends. Photons detected by the negatively angled collection fibers are intrinsically faint in comparison to their superficial counterparts, and this is echoed by the weakening signal as the tissue penetration grows deeper. The low signal could result in low signal-to-noise issues that may need to be corrected. To produce deep-tissue interrogation, the multiple-distance (SDSD) technique with an orthogonal fiber orientation offers greater signal than the negatively angled collection fibers presented. Therefore, for applications that demand high signal-to-noise ratio, the implantation of negatively angled fibers warrant caution and the SDSD method may be preferred. However, negatively angled fibers offer the advantage of compact probe sizes, since extended probing depths can be achieved at relatively smaller SDSD with negative-angle fibers.

Our data have shown that the obliquity of collection fibers in a fiber probe influences the depth selection of tissue reflectance. This additional degree of freedom allows more flexibility in fiber-probe design. Positively angled fibers can be used in conjunction with the single illumination-collection fiber for stronger reflectance acquisition in the epithelium. At the same time, negatively angled fibers can provide better tissue inter-

rogation in the deeper regions, such as for determination of hemoglobin saturation, neovascularization, and structural and biochemical information of stroma. Therefore, varying the angular orientation of collection fibers in a fiber optic probe offers greater probing-depth maneuverability than its flush-fiber counterparts.

Index-matching conditions at the tissue-fiber interface also play an important role in determining the expected probing depths of fiber probes. Data in Table 4 suggest that using glass as the index-matching material decreases the expected probing depths for fibers oriented at high angles. For collection angles less than 40 deg, such effects are negligible. This may be explained by refraction governed by Snell's law. As shown in Table 2, optical rotational angles of collection fibers may deviate from their physical rotational angles, and the magnitude and direction of the deflections depend on both fiber orientation and index mismatch across the tissue-fiber interface. When physical rotational angles are small (i.e., <40 deg), the resultant deflections of optical rotational angles are less significant. This may explain the negligible differences in the expected probing depths for fibers of lesser angles when different index-matching materials are used. However, optical rotational angles begin to significantly deviate from physical rotational angles when collection angles reach beyond 40 deg. Since the index of refraction of glass is greater than that of the tissue, the optical axes of fibers are effectively bent further away from the illumination, and the expected probing depths of fiber probes are consequently decreased.

Previously, we have referred to the correlation between the overlapping volume of the illumination and collection fibers and tissue depth selectivity. Numerical apertures, which define the half angles of optical fibers, affect the locations and volumes of such overlaps. As a result, the expected probing depth and detected reflectance of a fiber probe are influenced by fiber numerical apertures. For the orthogonal fibers and negatively angled fiber geometries, increasing the NA values would moderately reduce the expected probing depth, whereas an opposite effect was observed for the positively angled fiber geometry. When fibers are oriented perpendicu-

larly, increasing detection half angles allows more high-angle photons to be accepted by the fibers, and thus the overall expected probing depths decrease. On the other hand, when fibers are already obliquely oriented at high angles, increasing detection half angles primarily benefits the acceptance of photons that come from the deeper regions of the tissue and results in greater expected probing depths. However, from data shown in Table 4, the influence of fiber NA on spatial differentiation is not particularly significant, except for collection angles of 60 and 75 deg. According to Table 3, the changes in effective NA are likely too small to create significant modifications in the distribution of depth-resolved reflectance, especially for fibers oriented perpendicularly. For oblique fibers at angles greater than 40 deg, widening the half angle actually increases the expected probing depths, and we attribute this to the location of the illumination-collection overlap: as the fiber half angle broadens, a greater portion of the overlapping area protrudes downward and consequently enhances the detection of diffusely scattered photons from the bottom layer. Therefore, the center of gravity of reflectance detection shifts downward and results in greater expected probing depths in tissue.

All the evidence from our data indicates that early returning photons on the whole exit the tissue surface with greater exit angles. Modulating the detection of high-angle photons can effectively manipulate the probing depths and layer sensitivities of fiber probes. Using angularly resolved reflectance detection, one may effectively select the probing depths of fiber probes. As for the negatively angled fibers, the rationale is rejecting superficially scattered rays and only admitting photons with greater lateral displacements from the illumination spot. The probability for superficially scattered rays to be detected by negatively angled fibers is low. This is manifested in Figs. 3 and 4, where the detection of early returning rays was severely suppressed by the -25 -deg fiber.

In terms of implementation feasibility, there are some concerns that need to be addressed. Depending on applications and locations of suspect lesions, some *in vivo* measurements may pose a restriction on the sizes of fiber probes. Fiber rotation will indeed increase the sizes of fiber probes to avoid bending loss and plastic fractures of fiber optics. However, the oblique geometry does not necessarily require significant fiber rotation: facet beveling, to a certain extent, bends the optical axis of fiber optics, and when combined with minimal fiber rotation, one can achieve desired collection angles without overly expanding probe sizes. Direction-guiding prisms have been used in various side-viewing probes⁵⁶ and similar strategies can be applied here to reduce the probe size if necessary. Index matching also plays an important role in fiber bending: by affixing a glass plate between the fiber facets and tissue surface, one can effectively increase fiber's optical rotational angles, even when the physical rotation is limited. More importantly, the objective of this study is to demonstrate the strong correlations between spatial sensitivities and collection orientation. In the process of doing so, we should not limit ourselves to fiber optics: the concepts and results demonstrated in this study may be applicable to other potential probe technologies, such as specially tailored solid waveguides or on-chip CCD spectroscopy that embodies microscopic CCD sensors, as long as the fundamental principles of reflectance sampling remain the same.

5 Conclusion

This study investigates a variety of geometrical configurations for fiber optic probes to be used for optical spectroscopic measurements of epithelial tissue, with emphasis on the part of collection fibers. The fiber probes demonstrate markedly different tissue penetration capabilities, influencing the spatial profiles of the resultant reflectance spectra. With improved depth selectivity and discrimination, clinically valuable optical signals specific to biophysical tissue features may be more specifically measured.

The angular orientation of collection fibers in a fiber probe strongly influences the layer sensitivities of reflectance sampling in a multilayer tissue structure. Increasing collection angles in the positive direction results in stronger detection of superficially scattered photons, whereas collection fibers with negative angles have deeper tissue probing capability by rejecting the influence of superficially scattered rays and primarily detecting diffusely scattered photons from the bottom layer.

The lateral position of collection fibers relative to the illumination spot strongly influences the tissue layer selectivity of a fiber probe, and its trend is consistent for all angular orientations. Small SDS values lead to the superficial sampling of tissue, and greater probing depths can be achieved when greater SDS are utilized.

Among various orthogonal fiber configurations, the single illumination-collection fiber is most sensitive to the superficially scattered light. However, our simulations show that the epithelial-layer sensitivity of a fiber probe can be improved by implementing oblique collection fibers, even at SDS greater than 0. Given the tissue geometry and optical properties used in this study, stronger detections of the superficially scattered epithelial reflectance can be achieved with the oblique-fiber geometry than with their orthogonal counterparts. By using separate illumination and collection fibers, multiple collection fibers can be implemented simultaneously to increase reflectance detection. The depth selectivity in both epithelial and stromal layers can also be manipulated by modifying the angular orientation of the collection fibers with respect to the illumination axis without changing SDS.

Index matching also affects the probing capability of a fiber probe. We tested two possible index-matching materials—water ($n=1.33$) and glass ($n=1.5$). The refractive index of tissue in this study was set at 1.37, and thus water and glass in effect undermatched and overmatched the refractive index of the tissue, respectively. Due to the change in refractive indices across the tissue surface, the optical axes of fiber optics were deflected from their physical axes. Water, whose refractive index is less than that of tissue, reduces the angular deflection of an oblique fiber, whereas glass can effectively increase the fiber's collection angles calculated from the normal to tissue surface. Therefore, collection angles can be optimized by implementing appropriate index-matching materials.

In the final portion of this study, we investigate the effects of modifying the numerical apertures of collection fibers. We find that not only will numerical apertures influence the probing depths of a fiber probe, but their effects will also be dictated by other fiber geometrical parameters such as fiber obliquity and orientation. Increasing NA, in general, reduces

the expected probing depths of orthogonal and negative-angle fibers, but extends the expected probing depths of positive-angle fibers. For orthogonal and nearly orthogonal fibers, greater fiber half angles allow greater probabilities of detecting superficially scattered photons, which tend to exit the tissue surface with greater exit angles than the background signals. As a result, these fibers with greater NA values "see" more photons scattered in the superficial region as their collection cones expand toward the tissue surface. On the other hand, for highly oblique fibers, the expansion of fiber collection cones into the bottom tissue layer due to a greater NA value increases the intake of deeply scattered photons and consequently reduces the sensitivities to the epithelial layer located at shallow depths.

In summary, these investigations provide significant insight relevant to future probe designs for reflectance spectroscopy. Elastically scattered photons from the epithelial layer, which is relevant to the detection of epithelial precancerous lesions by methods such as reflectance spectroscopy, can be effectively sampled using oblique fiber geometries. The effectiveness of localized interrogation in the epithelium may be improved with positively angled collection fibers positioned at small source-detector separation distances, whereas the diffusely scattered signal from the stromal region can be better isolated using negatively angled collection fibers at greater SDSD. Fiber numerical apertures and index-matching conditions provide other potential means to fine tune the depth selectivity and layer sensitivities of fiber probes. With the foundation of this study, future efforts will focus on experimental verifications and specific strategies in probe fabrications to realize the proposed oblique-fiber designs.

Acknowledgments

Thanks to Vengadesan Nammalvar for his relentless intellectual support, and Nastassja Lewinski for her invaluable editorial assistance. This work is supported by Whitaker RG-02-0125, NIH R01CA09841-01A1, NSF BES 022-1544, NSF EEC 0118007, and National Institutes of General Medical Sciences Training Grant BM 08362.

References

- American Cancer Society, see http://www.cancer.org/docroot/STT/stt_0.asp.
- S. L. Robbins and V. Kumar, *Basic Pathology*, Saunders, Philadelphia, PA (1987).
- R. Cotran, V. Kumar, and S. Robbins, *Pathological Basis of Disease*, Saunders, Philadelphia, PA (1999).
- R. Drezek, R. Richards-Kortum, M. Brewer, M. Feld, C. Pitris, A. Ferenczy, M. Faupel, and M. Follen, "Optical imaging of the cervix," *Second Intl. Conf. Cervical Cancer*, pp. 2015–2027 (2003).
- U. Utzinger, M. Brewer, E. Silva, D. Dershenson, R. Blast, M. Follen, and R. Richards-Kortum, "Reflectance spectroscopy for *in vivo* characterization of ovarian tissue," *Lasers Surg. Med.* **28**, 56–66 (2001).
- P. Thueler, I. Charvet, F. Bevilacqua, M. Ghislain, G. Ory, P. Marquent, P. Meda, B. Vermeulen, and C. Depeursinge, "*In vivo* endoscopic tissue diagnostics based on spectroscopic absorption, scattering, and phase function properties," *J. Biomed. Opt.* **8**(3), 495–503 (2003).
- Y. Mirabal, S. Chang, E. Atkinson, A. Malpica, M. Follen, and R. Richards-Kortum, "Reflectance spectroscopy for *in vivo* detection of cervical precancer," *J. Biomed. Opt.* **7**(4), 587–594 (2002).
- G. Marquez and L. Wang, "White light oblique incidence reflectometer for measuring absorption and reduced scattering spectra of tissue-like turbid media," *Opt. Express* **1**, 454–460 (1997).
- K. Sokolov, R. Drezek, K. Gossage, and R. Richards-Kortum, "Reflectance spectroscopy with polarized light: is it sensitive to cellular and nuclear morphology," *Opt. Express* **5**, 302–317 (1999).
- J. R. Mourant, I. Bigio, J. Boyer, R. Conn, T. Johnson, and T. Shimada, "Spectroscopic diagnosis of bladder cancer with elastic light scattering," *Lasers Surg. Med.* **17**, 350–357 (1995).
- Z. Ge, K. Schomacker, and N. Nishioka, "Identification of colonic dysplasia and neoplasia by reflectance spectroscopy and pattern recognition techniques," *Appl. Spectrosc.* **52**, 833–839 (1998).
- F. Koenig, R. Larne, H. Enquist, F. McGovern, K. Schomacker, N. Kollias, and T. Deutsch, "Spectroscopic measurement of diffuse reflectance for enhanced detection of bladder carcinoma," *Urology* **51**, 342–345 (1998).
- M. Muller, T. Valdez, I. Georgakoudi, V. Backman, C. Fuentes, S. Kabani, N. Laver, Z. Wang, C. Boone, R. Dasari, S. Shapshay, and M. Feld, "Spectroscopic detection and evaluation of morphologic and biochemical changes in early human oral carcinoma," *Ame. Cancer Soc.* **97**, 1681–1692 (2003).
- G. Palmer, C. Zhu, T. Breslin, F. Xu, K. Gilchrist, and N. Ramanujam, "Comparison of multi-excitation fluorescence and diffuse reflectance spectroscopy for the diagnosis of breast cancer," *IEEE Trans. Biomed. Eng.* **50**, 1233–1242 (2003).
- T. J. Pfefer, L. Matchette, C. Bennett, J. Gall, J. Wilke, A. Durkin, and M. Ediger, "Reflectance-based determination of optical properties in highly attenuating tissue," *J. Biomed. Opt.* **8**, 206–215 (2003).
- I. Bigio and J. R. Mourant, "Ultraviolet and visible spectroscopies for tissue diagnostics: fluorescence spectroscopy and elastic-scattering spectroscopy," *Phys. Med. Biol.* **42**, 803–814 (1997).
- N. Ramanujam, "Fluorescence spectroscopy *in vivo*," in *Encyclopedia of Analytical Chemistry*, John Wiley and Sons, Chichester (2000).
- N. Ramanujam, M. Mitchell, A. Mahadevan, S. Thomsen, A. Malpica, T. Wright, N. Atkinson, and R. Richards-Kortum, "Spectroscopic diagnosis of cervical intraepithelial neoplasia (CIN) *in vivo* using laser-induced spectra at multiple excitation wavelengths," *Lasers Surg. Med.* **19**, 63–74 (1996).
- M. Canpolat and J. R. Mourant, "Particle size analysis of turbid media with a single optical fiber in contact with the medium to deliver and detect white light," *Appl. Opt.* **40**, 3792–3799 (2001).
- M. Canpolat and J. R. Mourant, "Monitoring photosensitizer concentration by use of a fiber-optic probe with a small source-detector separation," *Appl. Opt.* **39**, 6508–6514 (2000).
- T. Wright, R. Kurman, and A. Ferenczy, "Cervical intraepithelial neoplasia," in *Pathology of the Female Genital Tract*, A. Blaustein, Ed., Springer, New York (1994).
- B. Tromberg, "Optical and physiological properties of tumors," *OSA Annual Meeting* (1998).
- R. Drezek, M. Guillaud, T. Collier, I. Boiko, A. Malpica, C. Macaulay, M. Follen, and R. Richards-Kortum, "Light scattering from cervical cells throughout neoplastic progression: influence of nuclear morphology, DNA content, and chromatin texture," *J. Biomed. Opt.* **8**(1), 7–16 (2003).
- J. R. Mourant, A. Hielscher, A. Eick, T. Johnson, and J. Freyer, "Evidence of intrinsic differences in the light scattering properties of tumorigenic and non-tumorigenic cells," *Cancer* **84**, 366–374 (1998).
- J. R. Mourant, I. Bigio, D. Jack, T. Johnson, and H. Miller, "Measuring absorption coefficients in small volumes of highly scattering media: source-detector separations for which path lengths do not depend on scattering properties," *Appl. Opt.* **36**, 5655–5661 (1997).
- Y. Fawzi, A. Youssef, M. El-Batanony, and Y. Kadah, "Determination of optical properties of a two-layer tissue model by detecting photons migrating at progressively increasing depths," *Appl. Opt.* **42**, 6398–6411 (2003).
- K. Diamond, M. Patterson, and T. Farrell, "Quantification of fluorophore concentration in tissue-simulating media by fluorescence measurements with a single optical fiber," *Appl. Opt.* **42**, 2436–2442 (2003).
- J. R. Mourant, J. Freyer, A. Hielscher, A. Eick, D. Shen, and T. Johnson, "Mechanisms of light scattering from biological cell relevant to noninvasive optical-tissue diagnostics," *Appl. Opt.* **37**, 3586–3593 (1998).
- V. Backman, M. Wallace, L. Perelman, J. Arendt, R. Gurjar, M. Muller, Q. Zhang, G. Zonios, E. Kline, T. McGillican, S. Shapshay, T. Valdez, K. Badizadegan, J. Crawford, M. Fitzmaurice, S. Kabani, H. Levin, M. Seiler, R. Dasari, I. Itzkan, J. Tam, and M. Feld, "Detection of preinvasive cancer cells," *Nature (London)* **406**, 35–36

- (2000).
30. J. R. Mourant, T. Johnson, S. Carpenter, A. Guerra, T. Aida, and J. Freyer, "Polarized angular dependent spectroscopy of epithelial cells and epithelial nuclei to determine the size scale of scattering structures," *J. Biomed. Opt.* **7**(3), 378–387 (2002).
 31. K. Yong, S. Morgan, I. Stockford, and M. Pitter, "Characterization of layered scattering media using polarized light measurements and neural networks," *J. Biomed. Opt.* **8**(3), 504–511 (2003).
 32. A. Myakov, L. Nieman, L. Wicky, U. Utzinger, R. Richards-Kortum, and K. Sokolov, "Fiber optic probe for polarized reflectance spectroscopy *in vivo*: design and performance," *J. Biomed. Opt.* **7**(3), 388–397 (2002).
 33. A. Hielscher, J. R. Mourant, and I. Bigio, "Influence of particle size and concentration on the diffuse backscattering of polarized light from tissue phantoms and biological cell suspensions," *Appl. Opt.* **36**, 125–135 (1997).
 34. V. Backman, R. Gurjar, K. Badizadegan, I. Itzkan, R. Dasari, L. Perelman, and M. Feld, "Polarized light scattering spectroscopy for quantitative measurements of epithelial cellular structures *in situ*," *IEEE J. Sel. Top. Quantum Electron.* **5**, 1019–1026 (1999).
 35. J. R. Mourant, T. Johnson, and J. Freyer, "Characterizing mammalian cells and cell phantoms by polarized backscattering fiber-optic measurements," *Appl. Opt.* **40**, 5114–5123 (2001).
 36. J. R. Mourant, T. Fuselier, J. Boyer, T. Johnson, and I. Bigio, "Prediction and measurements of scattering and absorption over broad wavelength range in tissue phantoms," *Appl. Opt.* **36**, 949–957 (1997).
 37. S. Avriplier, E. Tinet, D. Etti, J. Tualle, and B. Gelebart, "Influence of emission-reception geometry in laser-induced fluorescence spectra from turbid media," *Appl. Opt.* **37**, 2781–2787 (1998).
 38. G. Kumar and J. Schmitt, "Optimal probe geometry for near-infrared spectroscopy of biological tissue," *Appl. Opt.* **36**, 2286–2293 (1997).
 39. T. J. Pfefer, L. Matchette, and R. Drezek, "Influence of illumination-collection geometry on fluorescence spectroscopy in multi-layered tissue," *Med. Biol. Eng. Comput.* **42**, 669–673 (2004).
 40. T. J. Pfefer, K. Schomacker, M. Ediger, and N. Nishioka, "Multiple-fiber probe design for fluorescence spectroscopy in tissue," *Appl. Opt.* **41**, 4712–4720 (2002).
 41. C. Zhu, Q. Liu, and N. Ramanujam, "Effect of fiber optic probe geometry on depth-resolved fluorescence measurements from epithelial tissues: a Monte Carlo simulation," *J. Biomed. Opt.* **8**(2), 237–247 (2003).
 42. T. J. Pfefer, L. Matchette, A. Ross, and M. Ediger, "Selective detection of fluorophore layers in turbid media: the role of fiber-optic probe design," *Opt. Lett.* **28**, 120–122 (2003).
 43. L. Quan and N. Ramanujam, "Relationship between depth of a target in a turbid medium and fluorescence measured by a variable-aperture method," *Opt. Lett.* **27**, 102–106 (2002).
 44. J. R. Mourant, J. Boyer, A. Hielscher, and I. Bigio, "Influence of the scattering phase function on light transport measurements in turbid media performed with small source-detector separations," *Opt. Lett.* **21**, 546–548 (1996).
 45. T. Papaioannou, N. Preyer, Q. Fang, A. Brightwell, M. Carnohan, G. Cottone, R. Ross, L. Jones, and L. Marcu, "Effects of fiber-optic probe design and probe-to-target distance on diffuse reflectance measurements of turbid media, an experimental and computational study at 337 nm," *Appl. Opt.* **43**, 2846–2860 (2004).
 46. M. Larsson, W. Steenbergen, and T. Stromberg, "Influence of optical properties and fiber separation on laser Doppler flowmetry," *J. Biomed. Opt.* **7**(2), 236–243 (2002).
 47. M. Larsson, H. Nilsson, and T. Stromberg, "In vivo determination of local skin optical properties and photon path length by use of spatially resolved diffuse reflectance with applications in laser Doppler flowmetry," *Appl. Opt.* **42**, 124–134 (2003).
 48. T. J. Pfefer, A. Agrawal, and R. Drezek, "Computational analysis of beveled-tip fiber probes for selective detection of subsurface fluorophores in turbid media," *Proc. SPIE* **5317**, 206–213 (2004).
 49. M. Skala, G. Palmer, C. Zhu, Q. Liu, K. Vrotsos, C. Marshak-Stone, A. Gendron-Fitzpatrick, and N. Ramanujam, "Investigation of fiber-optic probe designs for optical spectroscopic diagnosis of epithelial pre-cancers," *Lasers Surg. Med.* **34**, 25–38 (2004).
 50. L. Nieman, A. Myakov, J. Aaron, and K. Sokolov, "Optical sectioning using a fiber probe with an angled illumination-collection geometry: evaluation in engineered tissue phantom," *Appl. Opt.* **43**, 1308–1319 (2004).
 51. C. K. Brookner, M. Follen, I. Boiko, J. Galvan, S. Thomsen, A. Malpica, S. Suzuki, R. Lotan, and R. Richards-Kortum, "Autofluorescence patterns in short-term cultures of normal cervical tissue," *Photochem. Photobiol.* **71**, 730–736 (2000).
 52. R. Drezek, K. Sokolov, U. Utzinger, I. Boiko, A. Malpica, M. Follen, and R. Richards-Kortum, "Understanding the contributions of NADH and collagen to cervical tissue fluorescence spectra: modeling, measurements, and implications," *J. Biomed. Opt.* **6**(3), 385–396 (2001).
 53. S. Chang, D. Arifler, R. Drezek, M. Follen, and R. Richards-Kortum, "Analytical model to describe fluorescence spectra of normal and precancerous epithelial tissue: comparison with Monte Carlo simulations and clinical measurements," *J. Biomed. Opt.* **9**(3), 511–522 (2004).
 54. G. Zonios, R. Cothren, J. Arendt, J. Wu, J. Van Dam, J. Crawford, R. Manoharan, and M. Feld, "Morphological model of human colon tissue fluorescence," *IEEE Trans. Biomed. Eng.* **43**, 113–122 (1996).
 55. R. Hornung, T. Pham, K. Keefe, M. Berns, Y. Tadir, and B. Tromberg, "Quantitative near-infrared spectroscopy of cervical dysplasia *in vivo*," *Hum. Reprod.* **14**, 2908–2916 (1999).
 56. U. Utzinger and R. Richards-Kortum, "Fiber optic probes for biomedical optical spectroscopy," *J. Biomed. Opt.* **8**(1), 121–147 (2003).
 57. S. Bartel and A. Hielscher, "Monte Carlo simulations of the diffuse backscattering Mueller matrix for highly scattering media," *Appl. Opt.* **39**, 1580–1588 (2000).
 58. X. Wang, G. Yao, and L. Wang, "Monte Carlo model and light-scattering approximation of the propagation of polarized light in turbid media containing glucose," *Appl. Opt.* **41**, 792–801 (2002).
 59. Q. Liu, C. Zhu, and N. Ramanujam, "Experimental validation of Monte Carlo modeling of fluorescence in tissue in the UV-visible spectrum," *J. Biomed. Opt.* **8**, 223–235 (2003).
 60. L. Wang, S. Jacques, and L. Zheng, "Monte Carlo modeling of light transport in multi-layered tissue," *Comput. Methods Programs Biomed.* **47**, 131–146 (1995).
 61. S. Flock, M. Patterson, B. Wilson, and D. Wyman, "Monte Carlo modeling of light propagation in highly scattering tissues: model predictions and comparison with diffusion theory," *IEEE Trans. Biomed. Eng.* **36**, 1162–1173 (1989).
 62. A. Welch, C. Gardner, R. Richards-Kortum, E. Chan, G. Criswell, T. J. Pfefer, and S. Warren, "Propagation of fluorescent light," *Lasers Surg. Med.* **21**, 166–178 (1997).
 63. A. Gandjbakhche, R. Bonner, A. Arai, and R. Balaban, "Visible-light photon migration through myocardium *in vivo*," *Am. J. Physiol.* **277**, 698–704 (1999).
 64. A. Gandjbakhche and G. Weiss, "Descriptive parameter for photon trajectories in a turbid medium," *Phys. Rev. E* **61**, 6958–6962 (2000).
 65. G. Weiss and J. Kiefer, "A numerical study of the statistics of penetration depth of photons re-emitted from irradiated media," *J. Mod. Opt.* **45**, 2327–2337 (1988).
 66. R. Nossal, J. Kiefer, G. Weiss, R. Bonner, H. Taitelbaum, and S. Havlin, "Photon migration in layered media," *Appl. Opt.* **27**, 3382–3391 (1988).
 67. E. Okada, M. Firbank, and D. Delpy, "The effect of overlaying tissue on the spatial sensitivity profiles of near-infrared spectroscopy," *Phys. Med. Biol.* **40**, 2093–2108 (1995).
 68. R. Bonner, R. Nossal, S. Havlin, and G. Weiss, "Model for photon migration in turbid biological media," *J. Opt. Soc. Am. A* **4**, 423–432 (1987).